Self-driven ion deflectometry measurements using MeV fusion-driven protons and accelerated deuterons in the deuterated hybrid x-pinch on the MAIZE LTD generator

OPEN ACCESS
IOP Publishing
Plasma Physics and Controlled Fusion
Plasma Phys. Control. Fusion **66** (2024) 075021 (14pp)
https://doi.org/10.1088/1361-6587/ad5104

Self-driven ion deflectometry measurements using MeV fusion-driven protons and accelerated deuterons in the deuterated hybrid x-pinch on the MAIZE LTD generator

Vojtech Munzar[1,*], George Dowhan[2], Daniel Klir[1], Jan Novotny[1], Karel Rezac[1], Joe Chen[2], Jakub Cikhardt[1], Balzima Cikhardtova[1], Vojtech Juras[3], Nicholas Jordan[2], Pavel Kubes[1], Jakub Malir[1], Landon Tafoya[2], Karel Turek[4] and Ryan McBride[2]

[1] Faculty of Electrical Engineering, Czech Technical University in Prague, 16627 Prague 6, Czech Republic
[2] Department of Nuclear Engineering and Radiological Sciences, University of Michigan, Ann Arbor, MI 48109, United States of America
[3] Faculty of Nuclear Sciences and Physical Engineering, Czech Technical University in Prague, 16627 Prague 6, Czech Republic
[4] Nuclear Physics Institute, Academy of Sciences of Czech Republic, 18086 Prague 8, Czech Republic

E-mail: munzavoj@fel.cvut.cz

Received 4 March 2024, revised 6 May 2024
Accepted for publication 28 May 2024
Published 11 June 2024

Abstract

We report on the results of point-projection ion deflectometry measurements from a mid-size university z-pinch experiment. A 1 MA 8 kJ LTD generator at the University of Michigan (called MAIZE) drove a hybrid x-pinch (HXP) with a deuterated polyethylene fiber load to produce a point-like source of MeV ions for backlighting. In these experiments, 2.7 MeV protons were generated by DD beam-target fusion reactions. Due to the kinematics of beam-target fusion, the proton energies were down-shifted from the more standard 3.02 MeV proton energy that is released from the center-of-mass rest frame of a DD reaction. In addition to the 2.7 MeV protons, strongly anisotropic beams of 3 MeV accelerated *deuterons* were detected by ion diagnostics placed at a radial distance of 90 mm from the x-pinch. Numerical reconstruction of experimental data generated by deflected hydrogen ion trajectories evaluated the total current in the vacuum load region. Numerical ion-tracking simulations show that accelerated deuteron beams exited the ion source region at large angles with respect to the pinch current direction.

Keywords: ion deflectometry, proton imaging, z-pinch, hybrid x-pinch, ion acceleration, magnetic fields, deuteron beams

* Author to whom any correspondence should be addressed.

1. Introduction

Ion deflectometry is a diagnostic technique for measuring electric and/or magnetic (EM) fields based on the observed acceleration and/or deflection imparted on a probing ion beam. It is a reliable diagnostic tool for the study of strong transient EM fields in high energy density (HED) plasmas, especially in laser-produced plasmas [1]. In this technique, high-energy ion beams are emitted into a region of interest (the interaction region) to be deflected by the studied EM fields resulting in a distortion of the ion image, the deflectogram, recorded on the ion detector. The net ion deflections are manifested by the displacements of the detected ions on the detector with respect to their positions in the absence of EM fields. Because the ion deflections are gradual, the individual ion displacements are proportional to the strengths of the EM fields integrated along the individual ion paths, i.e. the path-integrated EM fields. The magnitudes of the ion displacements (and ion deflections) are inferred from the perturbed ion fluence or from the displacements of the fiducial features on the experimental deflectogram. In the literature, ion deflectometry is sometimes distinguished from ion radiography when the beam-plasma interactions are significant and need to be evaluated. However, the terms deflectometry and radiography are often used interchangeably. In the contemporary laser-generated plasmas, ion deflectometry/radiography is capable of visualizing of the EM fields while measuring their spatial distribution with μm-spatial and ps-temporal resolution, which is mainly determined by the size of the ion source and the duration of the ion emission, respectively.

This diagnostic method has not been fully developed for z-pinches, although z-pinch and laser-generated plasmas often utilize similar diagnostics. The main obstacle to its implementation in z-pinches is the generation of an adequate ion backlighting source (i.e. ion backlighter). In the classical deflectometry setup, the ion source must emit ion beams with: (*a*) high energy to avoid collisions with the plasma background (typically, several MeV for densities of HED plasmas); (*b*) a sufficient number of emitted ions able to reach the detector and generate an ion image of sufficient contrast; (*c*) a short duration of the ion burst compared to the temporal scale of the transient EM fields to obtain a clear image with a sufficiently short exposure; and (*d*) a high laminarity (the transverse position and velocity of each ion in the beam are linearly proportional to one another) ensuring that any distortion or displacement of the ion image can be unambiguously attributed to an ion ray deflected by local EM fields. In contemporary laser-plasma experiments, an ion (usually, proton) source satisfying these conditions is obtained by the interactions of a short-pulse high-power laser pulse with a target via ion accelerations, namely, the Target Normal Sheath Acceleration [2, 3], or via the fusion reactions (DD, D^3He, and T^3He) producing multi-MeV protons [4, 5]. Therefore, the first deflectometry experiments of z-pinch B-fields were conducted at facilities with access to intense lasers [6–8].

The first self-sustained deflectometry measurements of the z-pinch B-fields not requiring intense laser pulses were performed in 2019 on 3 MA deuterium hybrid gas-puff z-pinch driven by the GIT-12 generator [9]. In these experiments, a rapid current disruption of the plasma neck in the z-pinch generated strong transient electric fields that accelerated hydrogen ion beams up to energies of tens of MeV [10]. Although the ion source was proved to be not point-like [11], the ion deflectometry measurements were made possible by modifying the classical experimental setup and using the distant on-axis pinhole camera where the ion beams were projected through a nearly point-like aperture. In other words, the non-point-like ion emission of the ion source was circumvented by the point-like projection of the pinhole camera. Even though the maximum recorded energy of the hydrogen ions in these experiments reached up to 60 MeV [12], almost all results of the deflectometry measurements were based on recorded data of the 2.3 MeV deuteron beams. Since hydrogen beams with comparable energies were detected on the 1.4 MA MAGPIE facility at Imperial College London in the UK [13], and on the 0.7 MA HAWK facility at the Naval Research Laboratory in Washington, D.C., USA [14], the ion deflectometry measurements seem feasible at university-scale pulsed-power devices with much lower stored energies and currents than GIT-12 without requiring intensive lasers.

This paper represents another step toward the implementation of ion deflectometry in z-pinches by introducing and verifying the concept of a point-like ion source generated by the hotspot of a hybrid x-pinch (a micro z-pinch) producing MeV fusion protons and accelerating 3 MeV deuteron beams. In addition, this paper presents deflectrometry-based measurements of the load current in a mid-size pulsed-power device, a 1 MA 8 kJ linear-transformer-driver (LTD) generator (called MAIZE) at the the University of Michigan, MI, USA [15, 16]. Experimental results from neutron and x-ray detectors used in the same experimental campaign are presented in [17].

The paper is organized as follows: section 2 introduces the basics of ion deflectometry in azimuthal B-fields. Section 3 introduces the experimental setup of the hybrid x-pinch at MAIZE. Section 4 presents experimental results and their discussions. Section 4.1 presents the experimental results from the neutron time-of-flight (nToF) and diamond photoconductive diode (PCD) detectors, the fast framing cameras (FFC), and the ion step-wedge-filter spectrometer. These results provide information about the energies of detected neutrons, x-rays, and ions. Based on the experimental evidence, deuteron beams were accelerated up to $>$3 MeV energies. Section 4.2 shows the experimental images of 2.7 MeV protons and 3 MeV deuterons. In two shots, we estimate the total pinch current and the size of the deuteron and proton source by evaluating the ion deflections via numerical ion tracking simulations. Section 4.3 discusses the specific angular distribution of the simulated deuteron and proton beams, which was emitted at large divergence angles. Conclusions of the experimental results and future prospects are provided in section 5.

2. Basics of ion deflectometry in the z-pinch geometry

In figure 1(a), we present the basic principles of ion deflectometry in the azimuthal magnetic field $\mathbf{B}_\varphi$ of an azimuthally symmetric z-pinch plasma. A laminar ion beam is fired from a point-like source into the B-field region where the ions undergo continuous lateral deflections caused by the magnetic Lorentz force $\mathbf{F} = Q\mathbf{v} \times \mathbf{B}$, where Q and $\mathbf{v}$ are the ion charge and velocity, respectively, until they are finally deflected from their initial direction by a net deflection angle α. After leaving the B-fields, the deflected ions travel balistically to the ion detector (typically a filtered stack of radiochromic films [18–20] or CR-39 track detectors [21, 22]), which records the spatial distribution of the deflected ion beam, i.e. an ion-beam profile image. This image manifests the net displacements of individual ion rays caused by the deflection of their trajectories in the studied B-fields. To evaluate the ion displacements $\Delta\xi$, the recorded ion image is compared with a reference image representing the ion beam's profile in the absence of B-fields. This reference ion image is obtained either from the known beam profile prior to the deflections, or by placing a fiducial object with distinctive features (usually, a solid grid called a deflectometry grid or the D-grid) between the ion source and the B-field region.

Inside the B-field region, the Lorentz force acts on each individual ion ray, changing its direction but not its energy. Therefore, after an arbitrarily long time interval between t_0 and t_1, the ion velocity vector $\mathbf{v}$ is rotated from the initial direction $\mathbf{v}_0 \equiv \mathbf{v}(t_0)$ to $\mathbf{v}_1 \equiv \mathbf{v}(t_1)$ but its magnitude is kept constant ($\|\mathbf{v}_0\| = \|\mathbf{v}_1\|$). We can characterize this rotation by a velocity shift vector $\Delta\mathbf{v} \equiv \mathbf{v}_1 - \mathbf{v}_0$ (see figure 1(b)), which is given by the integral of the magnetic force

$$\Delta\mathbf{v} = \frac{Q}{m}\int_{t_0}^{t_1} \mathbf{v} \times \mathbf{B}\mathrm{d}t. \tag{1}$$

In practice, it is impossible to follow deflected ion trajectories in time, so it is convenient to parameterize the integral in equation (1) with an ion path length ℓ instead of the time variable t, and then, write

$$\Delta\mathbf{v} = -\frac{Q}{m}\int_0^L \mathbf{B} \times \mathrm{d}\boldsymbol{\ell}, \tag{2}$$

where $L = \int_{t_0}^{t_1} v\mathrm{d}t$ is a total length of the deflected ion trajectory and $\mathrm{d}\boldsymbol{\ell} = \mathbf{v}\mathrm{d}t$ is its oriented path element. The integral on the right side of equation (2), referred to as the path-integrated or line-integrated B-fields, represents the sum of the continuous ion rotations, characterized by the deflection angle α, and the cumulative effect of the B-fields on individual passing ions. The dependence between the magnitude of the path-integrated B-fields and the deflection angle α is given by the general magnetic deflection equation [23], derived from equation (2) as follows

$$\sin\left(\frac{\alpha}{2}\right) = \frac{\|\Delta\mathbf{v}\|}{2v} = \frac{Q}{2mv}\left\|\int_0^L \mathbf{B} \times \mathrm{d}\boldsymbol{\ell}\right\|. \tag{3}$$

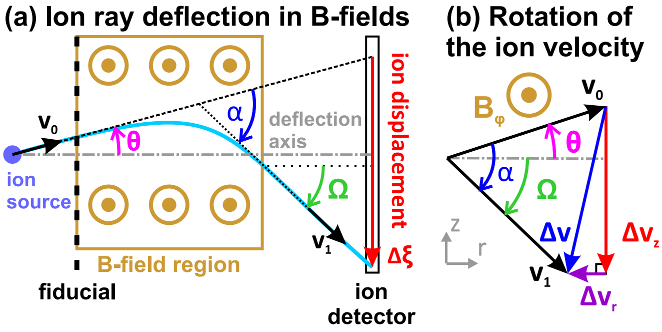

Figure 1. (a) A schematic illustrating the basic principles of ion deflectometry in magnetic fields. After an ion ray is emitted from the ion source into the B-field at the initial (divergence) angle θ and passes through the B-field region, its initial direction is rotated by the deflection angle α and it reaches the ion detector plane at the final (observation) angle Ω. (b) A cartoon illustrating the rotation of the ion velocity vector in B-fields during ion deflection.

The deflection half-angle $\alpha/2$ in equation (3) comes from the bisection of the ion velocity triangle (illustrated in figure 1(b)), which is always isosceles due to the constant velocity magnitude and can therefore be divided into two right triangles, where we can apply trigonometric functions.

Since it is usually difficult to estimate the spatial dimensions of the specific B-fields to calculate their magnitude, the evaluation of the magnitude of the path-integrated B-fields $\|\int \mathbf{B} \times \mathrm{d}\boldsymbol{\ell}\|$ or its components are the fundamental quantities provided by standard ion deflectometry measurements.

Assuming only azimuthal B-fields $\mathbf{B}_\varphi$, path-integrated B-fields $\int_0^L \mathbf{B}_\varphi \times \mathrm{d}\boldsymbol{\ell}$ have only two non-zero components $\int_{z_0}^{z_1} B_\varphi \mathrm{d}z$ and $-\int_{r_0}^{r_1} B_\varphi \mathrm{d}r$, where $z_0 = z(t_0)$, $z_1 = z(t_1)$, $r_0 = r(t_0)$, and $r_1 = r(t_1)$. Then, equation (2) leads to corresponding deflection equations for the components of the velocity shift Δv_r and Δv_z

$$\Delta v_r = v(\cos\Omega - \cos\theta) = -\frac{Q}{m}\int_{z_0}^{z_1} \mathrm{B}_\varphi \mathrm{d}z \tag{4}$$

and

$$\Delta v_z = v(\sin\Omega - \sin\theta) = \frac{Q}{m}\int_{r_0}^{r_1} \mathrm{B}_\varphi \mathrm{d}r. \tag{5}$$

Equations (4) and (5) describe the ion velocity shifts using only the angular rotation of the ion velocity from the initial and final angles θ and Ω (see figure 1(b)). We define θ and Ω as oriented angles from the deflectometry axis, a line perpendicular to the ion detector. The angle θ corresponds to the initial divergence of the ion beam so we call it the divergence angle. The angle Ω is an angle of incidence at which the ions are detected, so we call it the observation angle. The orientation of θ and Ω depends on the direction of the initial and final velocity vectors $\mathbf{v}_0$ and $\mathbf{v}_1$ with respect to the deflection axis, respectively. The deflection angle α is given by the difference between the initial and final angles $\alpha = \Omega - \theta$. It is oriented in the same direction as the observation angle Ω. This means that if the ion is deflected in the opposite direction to the initial divergence angle θ (see the example in figure 1(a)) and

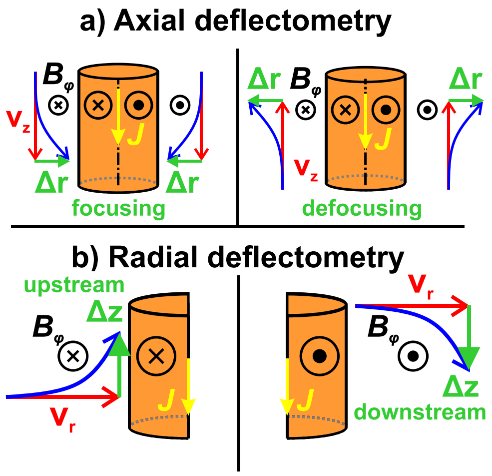

Figure 2. Fundamental ion deflections in the cylindrical azimuthal B-fields of a z-pinch. (a) Axially propagating ions are deflected radially by azimuthal B-fields. Depending on whether the ions pass through azimuthal B-fields in or against the direction of the current (i.e. downstream or upstream), they are deflected either toward or away from the pinch axis (i.e. focused or defocused). (b) Radially ions traveling are deflected axially by azimuthal B-fields. Depending on whether the ions are propagating radially toward or away from the z-pinch axis, they are deflected either in or against the direction of the current (i.e. downstream or upstream).

reaches the ion detector on the opposite side of the deflection axis, the deflection strength is equal to the sum of both angles and $|\alpha| = |\Omega| + |\theta|$.

Based on the direction of the deflectometry axis, there are two fundamental configurations of ion deflectometry in azimuthal B-fields of the symmetric z-pinch, that is, the axial and radial deflectometry (see in figure 2). In the axial deflectometry (figure 2(a)), the ions propagate axially through the azimuthal B-fields, and thus the deflecting force is predominantly radial ($F_r = Qv_z\mathrm{B}_\varphi$), producing the radial displacements Δr proportional to the path-integrated B-fields $\int_{z_0}^{z_1} \mathrm{B}_\varphi\,\mathrm{d}z$. The radial displacements lead to the focusing of the ion beam ($\Delta r < 0$) if it is directed downstream with respect to the direction of the z-pinch axial current density $\mathbf{J}$, or lead to its defocusing ($\Delta r > 0$) if it is directed upstream. In the radial deflectometry (figure 2(b)), ions propagate radially through the azimuthal B-fields, and thus the deflecting force is predominantly axial ($F_z = -Qv_r\mathrm{B}_\varphi$), producing the axial displacements Δz proportional to $\int_{r_0}^{r_1} \mathrm{B}_\varphi\,\mathrm{d}r$. The axial ion displacements are upstream when the ions move toward the z-pinch axis or downstream when they move away from it.

Our analysis [23] of the general principles of ion deflectometry in z-pinch B-fields and later the experimental measurements [9] have demonstrated that the ion beams fired axially into the z-pinch can investigate the specific distribution of the B-fields inside the z-pinch. To map the magnetic fields along the z-pinch axis, the electrodes must be permeable for passing ions from the ion source and to the ion detector. This is possible in specific z-pinch configurations, where the electrodes are in the form of meshes (for example, in gas puffs) or do not face each other (for example, in plasma focuses). However, in the classical experimental configuration of z-pinches (or x-pinches), the electrodes are solid, and access to the plasma along the z-axis is limited. Therefore, in that case, azimuthal B-fields can be probed only in the radial direction. Accordingly, the first deflectometry measurements (in 2012 [6] and 2014 [7]) in z-pinches were performed in the radial configuration. The downside of the radial deflectometry is that ions emitted radially must transverse vacuum B-fields around the z-pinch plasma before reaching it and after leaving it (see figure 2(b)). Because the ion path in these external B-fields are much longer than inside the z-pinch plasma, ions are deflected by the vacuum B-field much more than by the internal B-fields. It means that the specific distribution of the z-pinch current density affects the experimental data only marginally. The upside of predominant influence of the external B-fields is that the B-fields outside the cylindrical conductor have a known profile $\mathrm{B}_\varphi = \mu_0 I/2\pi r$, where μ_0 is the permeability and I is the pinch current. Assuming that the ions do not pass the z-axis, we can calculate the path integral on the right-hand side of equation (5) as follows

$$\Delta v_z = v\left(\sin\Omega - \sin\theta\right) = \frac{Q}{m}\frac{\mu_0 I}{2\pi}\ln\left(\frac{r_1}{r_0}\right). \qquad (6)$$

Therefore, the ion deflections are determined by only one non-geometric parameter: the total z-pinch current I. Furthermore, it follows from equation (6) that the velocity shift Δv_z and the deflection angles α are identical for all ions in B-fields of the symmetric z-pinch with the given current I. This means that ions emitted in the r-z plane with comparable radial velocities will be deflected by a similar amount, resulting in nearly uniform ion displacements in the detector plane, shifting the deflectogram in the ion detector as a whole without significant distortion. Due to the almost uniform ion displacements, the radial ion beams stay predominantly laminar throughout their deflections and fall onto the detector as if projected ballistically from a small virtual source. Therefore, the net displacement of the ion beam in the detector plane corresponds to a shift of the virtual source to the opposite direction. Moreover, due to the uniform ion displacements in the deflectogram, the radial deflectometry measurements in the azimuthally symmetric setup require only a small number of identified points in the recorded deflectogram to determine its vertical shift.

3. Experimental configuration on the MAIZE generator

Our experiments were performed using the LTD generator MAIZE with the low inductance of 20 nH and stored energy of 8 kJ [16]. We proposed that the MAIZE generator is capable of driving a point-like ion deflectometry source of MeV protons produced via beam-target fusion reactions due to deuteron beams emitted from hot dense plasmas reacting with the target plasmas. For this purpose, the experimental load of MAIZE was a deuterated polyethylene $[C_2D_4]_n$ fiber (or simply, a CD_2 fiber) arranged in an experimental configuration of a hybrid x-pinch.

The hybrid x-pinch represents a simplified concept of a classical x-pinch. Classical wire x-pinches [24, 25] are made by crossing several thin wires of high Z materials (e.g. tungsten). When a high current passes through them, they begin to ablate and create hot dense plasmas at the crossing point of the x-pinch, called the hot-spot, which emits intense soft x-ray (SXR) radiation. Accordingly, the classical wire x-pinches are commonly used for point projection x-ray radiography [26–29]. In the hybrid x-pinch (HXP) configuration [30–32], the X-shape of the x-pinch is formed by the conical shape of the solid electrodes instead of the crossed wires. Moreover, the crossing point of the classical wire x-pinch, i.e. the x-point, is replaced by a narrow (≈0.5–3 mm) gap between the tips of the electrode inserts connected by a thin CD_2 fiber. When the voltage is applied, the current flashes rapidly across the surface of the fiber, which begins to ablate and transform into a localized hot dense carbon-deuterium plasma, called a micro-z-pinch, similar to the micro-pinch that forms in the classical wire-based x-pinch. The electrode inserts in the hybrid x-pinch must be hollow along the z-axis to allow the ablated plasma to flow out of the crossing region. The length of the electrode gap must be small to avoid secondary hot-spot formation. The advantages of hybrid x-pinches over classical wire-based x-pinches are that hybrid x-pinches are simpler to construct and field experimentally and possibly easier to model due to the simpler (cylindrically symmetric) geometry. For the purposes of ion backlighting, an essential feature of the hybrid x-pinch configuration is that it can drive loads of almost any material, including low-conductivity deuterated polyethylene plastic, due to the small distance between the tips of the electrode inserts.

For the optimal ablation rate and the formation of the hot spot, the current rate $\mathrm{d}I/\mathrm{d}t$ of the generator must be for both classical and hybrid x-pinches matched to the optimal linear mass density of the experimental load. Typically, >1 kA ns^{-1} is required, and therefore MAIZE is well suited for x-pinch experiments. Note that MAIZE's relatively low inductance allows rapid energy delivery into the load.

The cross-sectional schematic of the experimental setup on MAIZE is shown in figure 3. The current was delivered from the capacitor bank through the magnetically insulated transmission lines (MITL) to the load region. In the load region, the current propagated along four 12.8 mm thick axisymmetrically arranged stainless steel posts, called the return current rods, located at radial positions that were 64.5 mm from the setup axis. After the rods, the current continued through the outer part of the anode, a stainless-steel plate, and then converged onto the central conical electrode inserts installed to reduce the anode-cathode (AK) electrode gap from ≈24.5 mm to 1–3 mm. The half-angle of the electrode cone was ≈50°. The deuterated polyethylene fiber connecting the electrodes (see figure 3(b)) was stretched through the holes drilled inside the electrode inserts. Due to the small distance between the tips of the conical electrode inserts, the electrical current ran through only a short length of fiber, creating the micro-pinch. After leaving the load region, the current was diverted back

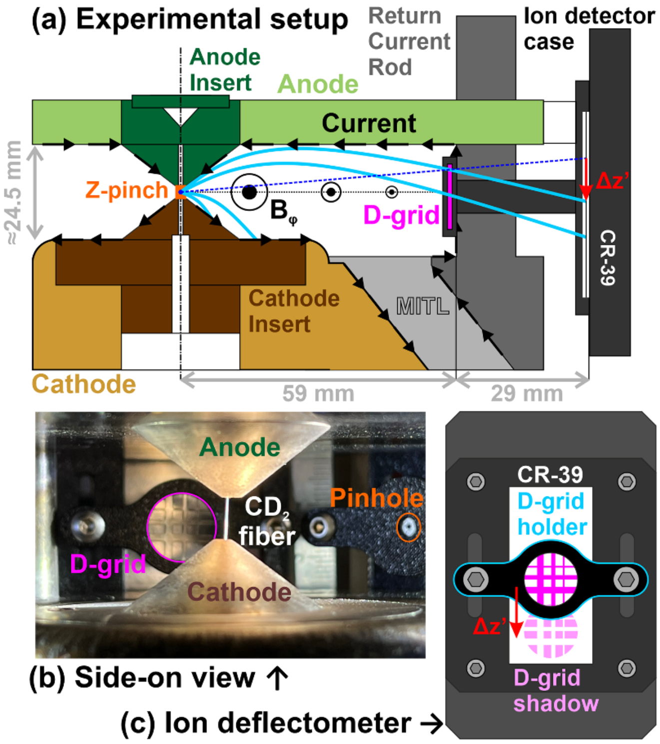

Figure 3. (a) Experimental setup of the radial deflectometry measurements using the point-like ion source driven by the CD_2 fiber hybrid x-pinch performed on the MAIZE LTD generator. (b) Side view of the conical electrodes and plastic holders for the D-grid and the pinhole disk of the installed ion deflectometer and pinhole camera, respectively. The photo was taken before the vacuum pumping of the experimental load region which pushed the electrode inserts closer together than shown (namely, to the 2.8 mm distance stated in the text). (c) Side view of the ion deflectometer showing the vertical shift of the shadow of the deflectometer grid (D-grid) in the detected ion signal caused by deflections of ions in the B-fields.

into the MITL. The hot dense carbon-deuterium plasmas generated from the ablated CD_2 fiber provided a highly localized source of MeV protons via DD beam-target fusion reactions. They allowed us to perform *in-situ* radial deflectometry measurements of the x-pinch current.

To capture the ion deflections, a fiducial deflectometry grid (i.e. the D-grid) cut from a 1 mm thick CR-39 plastic was placed between the electrodes at a radial distance of 59 mm from the axis (see figure 3(a)). The grid lines of the D-grid were 0.4, 0.9, and 1.4 mm thick and were separated by a 1.6 mm distance (see figure 3(b)). The D-grid was inserted into a circular slot inside a round plastic holder, which was connected to an ion detector case by two 7 mm thick rods (see figure 3(a)). The radius of the holder was 8.4 mm. The ion detector with a piece of the CR-39 plastic was placed 29 mm behind the D-grid holder and inside the ion detector case. It displayed the image of the deflected ion beam with the imprinted D-grid shadow (see figure 3(c)). Since ions propagated radially outward through azimuthal B-fields (see illustrated ion trajectories in figure 3(a)), the ion beam was displaced

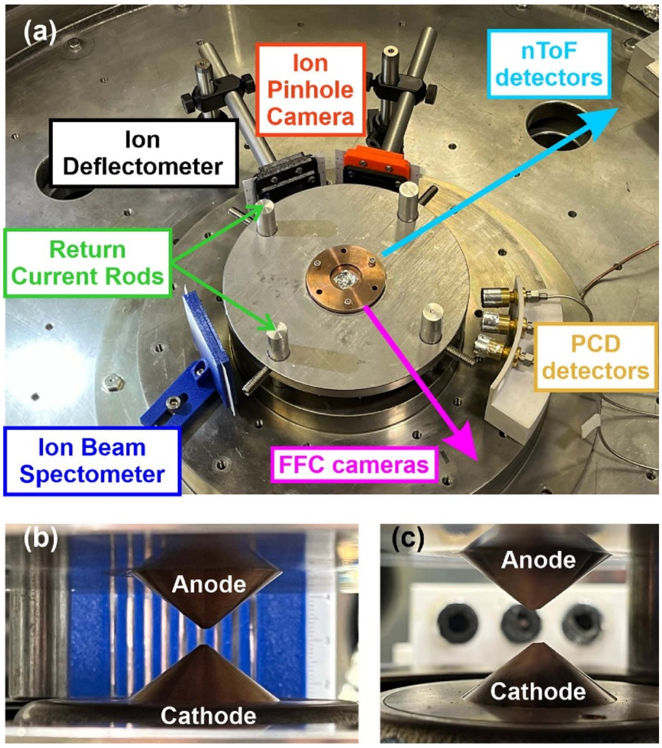

Figure 4. (a) The layout of diagnostics investigating the ion, neutron, visible light, and x-ray emission of the CD_2 fiber hybrid x-pinch. Side-view of the conical electrodes before the vacuum pumping with the line of sight directed (b) toward the ion beam spectrometer and (c) towards the PCD detectors.

axially downstream (in the direction of the current). From the vertical displacement of the D-grid shadow $\Delta z'$ in the recorded ion beam (see figure 3(c)), we could evaluate the total pinch current I at the time of ion emission.

The measurements of the ion displacements from the experimental ion images require the reference ion image. The D-grid installed relatively far from the ion source ($\approx$59 mm) to avoid possible breakdown of the AK gap could not capture the initial directions of ion beams before deflection. Thus, we could not establish the initial beam profile. Instead, we reconstructed the reference image from a geometric projection of the D-grid image without any B-fields onto the detector plane. The ion displacements $\Delta z'$ (see figure 3(a)) evaluated this way represented only a part of the actual ion displacements $\Delta\xi$ illustrated in figure 1. However, they still unambiguously indicated the ion deflections.

Besides the detector measuring ion deflections, called the ion deflectometer, additional diagnostics were installed on MAIZE to analyze the ion emission and the x-pinch plasmas (see figure 4(a)). The ion beam spectrometer shown in figure 4(b) measured the energy and anisotropy of the ion emission. In addition to the ion spectrometer, we used an ion pinhole camera detector to study the ion source. The pinhole camera was installed at the same distance from the ion source as the ion deflectometer and with the identical plastic holder. In contrast to the ion deflectometer, the circular slot inside the plastic holder of the pinhole camera contained a small 0.5 mm thick lead sheath, into which a 0.6 mm wide circular pinhole, i.e. the aperture of the pinhole camera, was pierced. Since the plastic holder did not cover the entire CR-39 detector behind it, the pinhole camera detector could not only detect ions passing through the pinhole and thus capture the image of the ion source, but also detect ions traveling around the plastic holder and thus capture the partial image of the ion beam. Given the size of the pinhole and the magnification of 0.49, these two images could not overlap for any realistic ion source size.

In addition to the ion emission, three types of diagnostics detected the light radiation from the hot plasmas. A FFC captures images of the x-pinch plasmas in the visible light spectrum. Three fielded diamond PCD detectors shown in figure 4(c) measured the temporal distribution of the emission of $\gtrsim$1 keV x-rays. The neutron yields were determined by two types of detectors. The first one was the beryllium neutron activation detector relying on the $^9\mathrm{Be}(\mathrm{n},\alpha)^6\mathrm{He}$ reaction and the subsequent β^- decay of ^{6}He. The second type of installed neutron detector was Bubble Detector-Personal Neutron Dosimeters (BD-PNDs) [33, 34]. These detectors utilize a superheated fluid that vaporizes and produces bubbles after absorbing a defined dose of neutron radiation. The calibrated sensitivity of the BD-PNDs was $\approx$15 bubbles/mrem, which corresponds to a dose of 29×10^6 $\mathrm{n} \cdot \mathrm{cm}^{-2} \cdot \mathrm{rem}^{-1}$ assuming a monoenergetic 2.45 MeV DD neutron emission. Finally, the time-resolved hard x-ray and neutron diagnostic was provided by two nToF scintillator detectors. The total load current was measured by a Rogowski coil residing in a slot cut into the anode surface of the power feed, at a major radius of 11 cm. The additional diagnostics used on MAIZE during this experimental campaign are presented in [17].

4. Experimental results of shots 3010 and 3012

In the configuration of the hybrid x-pinch with the CD_2 fiber load, we performed 18 shots in total. The anode-cathode gap and the fiber diameter varied from 1.6 mm to 3.4 mm and from 80 μm to 160 μm, respectively. The average neutron yield was $(15.6 \pm 9.6) \times 10^6$. However, this section focuses on the experimental results obtained in two most important shots, namely, shots 3010 and 3012.

In shots 3010 and 3012, the measured neutron yields were the highest, $\approx 1.4 \times 10^8$ and $\approx 2.8 \times 10^7$, respectively, and the ion signals of recorded deflectograms were the strongest (see figure 5). The experimental setup was the same for both shots. The output voltage was 140 kV, and the total circuit current reached $\approx$500 kA with a rise time of $\approx$200 ns. The distance between the conical electrode tips after the vacuum pumping was set at $\approx$2.8 mm. The thickness and mass density of the used polyethylene fiber were $\approx$160 μm and $\approx$0.9 g/cm^{-3}, respectively. The CR-39 detectors in the ion deflectometer and the pinhole camera were both covered by 50 μm thick aluminum detector absorbers.

Figure 5(a) shows the CR-39 detector used in the ion deflectometer in shot 3010. The recorded ion fluence is by

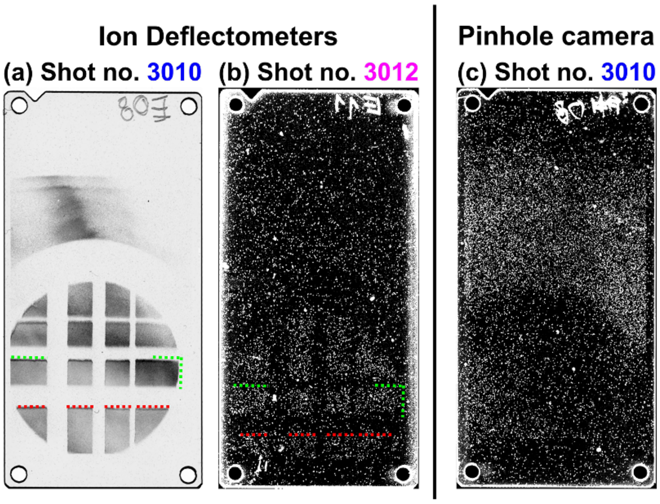

Figure 5. Experimental ion deflectograms captured by CR-39 detectors used by the ion deflectometer in shots 3010 and 3012 and the ion pinhole in shot 3010. The CR-39 images (b) and (c) were inverted and their contrast was enhanced to reveal shadows in the faint background signal produced by fusion protons. In (a), the distinct and sharp signal was produced by the anisotropic deuteron beams and recorded by the ion deflectometer in shot 3010. In (b), a faint D-grid shadow was produced by fusion protons recorded by the ion deflectometer in shot 3012. Red and green dotted lines in (a) and (b) are used to indicate similar features of the D-grid shadow. (c) The shadow of the plastic pinhole holder in the proton background captured by the ion pinhole camera's CR-39 detector in shot 3010.

order of magnitude higher than in other shots. The D-grid shadow in the deflectogram is distinct and quite sharp. Since the ion deflectometer is an integrated diagnostic, the sharpness of the D-grid shadow indicates (*i*) the short duration of the ion backlighting compared to the evolution of the deflecting B-fields and (*ii*) that the ions were projected onto the CR-39 from a small virtual source. From the thickness of the horizontal penumbra of the D-grid shadow, the radial width of the virtual ion source was ≈0.2 mm. The height of the virtual ion source estimated from the vertical penumbra was ≈0.6 mm. Because the assumed ion deflections in the B-field outside the x-pinch were nearly uniform and moderate, the ion beam was predominantly laminar. Therefore, we can assume that the spatial scales of the virtual ion source corresponded to the spatial dimensions of the real ion source in the x-pinch. However, in the vertical (axial) direction, the ion image could have also been influenced to some extent by the temporal evolution of the deflecting B-fields.

The spatial distribution of the ion fluence in the deflectogram in shot 3010 was highly anisotropic and, hence, contrasting to the more uniform and expected distribution of the beam-target-fusion-driven proton beams. Interestingly, such a uniform ion signal was captured in this shot by the ion pinhole detector (see figure 5(c)). Due to the low recorded ion fluence, this CR-39 detector was thoroughly cleaned; then, its scanned image was digitally inverted, and its contrast significantly increased to visualize the faint ion signal. There was no visible signal behind the pinhole itself, probably due to the low fluence of the proton beam. Nevertheless, we observed a shifted shadow of the pinhole holder (identical to the D-grid holder illustrated in figure 3(c)), manifesting the displacements of deflected ions. The lack of the strong ion signal in this CR-39 detector hinted the anisotropy of the ion emission in shot 3010 observed by the ion deflectometer. The pinhole camera was adjacent to the ion deflectometer (see the side-view in figure 3(b)), and still, the ion fluence detected by the pinhole camera detector was significantly lower than in the ion deflectogram shown in figure 5(a). Similarly uniform and low-fluence ion signal was captured by the ion deflectometer in shot 3012 (see figure 5(b)). In the inverted and enhanced CR-39 image, a diffusive shadow of the D-grid appeared in the ion background. For easier recognition of the D-grid shadow, its distinctive features, i.e. the partial frames of the grid gaps and the lower edge of the thickest grid line, were highlighted by green and red dotted lines, respectively.

Actually, the anisotropy of the ion emission detected by the ion deflectometer in shot 3010 was only one of several observations that led us to conclude that the intense ion signal in this shot originated from deuteron beams accelerated by strong induced electric fields generated by a rapid disruption of the z-pinch current, and that the diffusive ion signals recorded in this shot by the pinhole detector and in shot 3012 by the ion deflectometer were produced by beam-target DD-fusion protons. Other evidence for this hypothesis based on experimental results of multiple diagnostics in shot 3010 is presented in the following subsection.

4.1. Experimental results from non-deflectometry diagnostics in shot 3010

In addition to the anisotropy of the ion signal, further evidence for multi-MeV deuterons in shot 3010 was provided by the experimental data of the nToF detectors and their comparison with the obtained data from the PCD detectors.

The nToF detectors in shot 3010 were placed at a radial distance of 1 and 2 meters from the x-pinch, and were shielded by a 5.4 cm thick lead brick and a 1.3 cm thick lead plate, respectively. As shown in figure 6(a), both nToF detectors in this shot were saturated despite the strong shielding of the near detector and the greater distance from the x-pinch of the far one. Nevertheless, in the signal from the far nToF detector, we can see two clipped signal peaks, which were separated by a moderate signal dip. Since the nToF detector can detect both hard x-ray or fast neutron emissions, we needed to determine which emission produced which peak in the far nToF detector's signal. In general, x-ray photons can be distinguished from the fast neutrons due to their different velocities leading to the different travel times. However, this requires additional information about the time of the x-ray and neutron emission. To that end, we investigated signals of three PCDs (see figure 6(b)) installed at a radial distance of ≈100 mm from the x-pinch. Note that the signals from the nToF and PCD detectors were synchronized to exclude all delays caused by the signal processing.

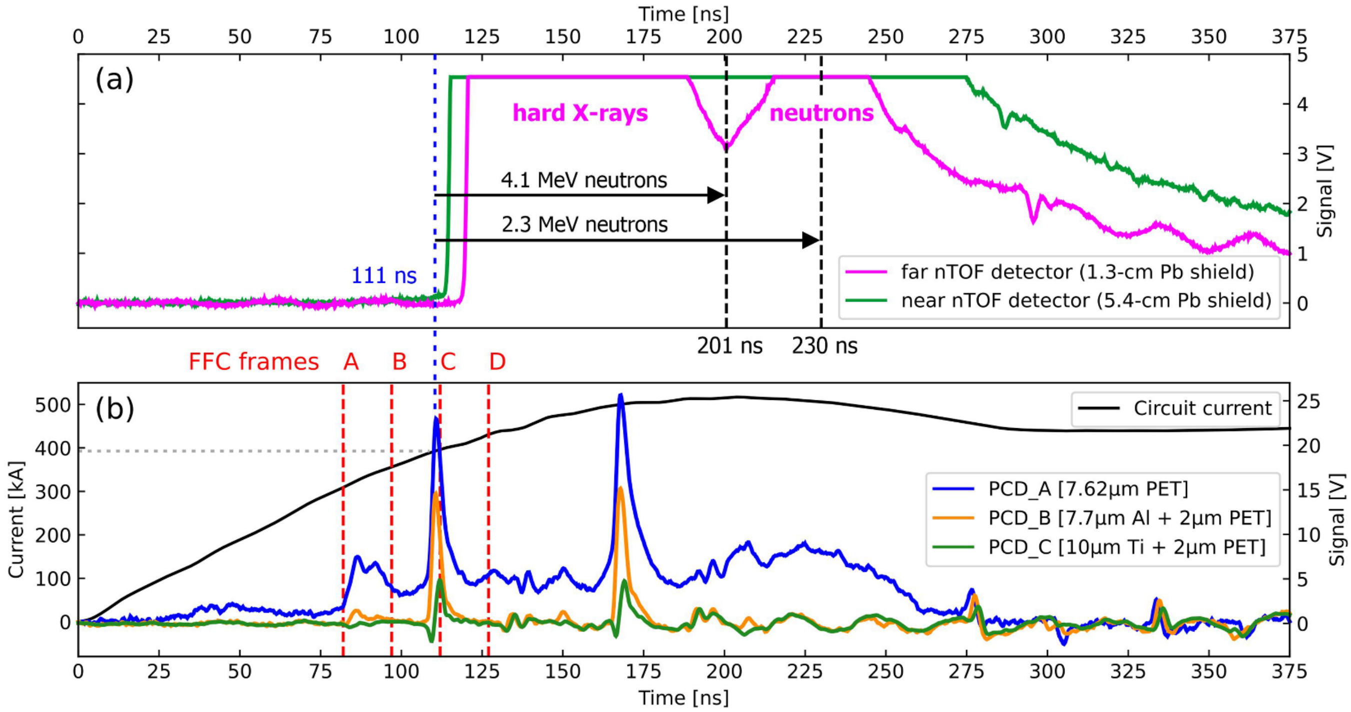

Figure 6. Signal data from shot 3010. (a) Signal traces of neutron time-of-flight (nToF) scintillator detectors installed at radial distances of 1 and 2.5 m from the x-pinch and protected by 5.4 cm and 1.3 cm thick lead shielding, respectively. (b) Traces of the circuit current (in black) and the PCD detectors (in blue, orange, and green) synchronized with the time stamps of selected FFC frames (in red). The first and the second clipped peaks in the nToF signal correspond to the 0.6 MeV x-rays and the 4.1 MeV neutrons, respectively, both emitted at the approximate time of the first x-ray pulse recorded by the PCD detectors, i.e. the x-ray pulse closest to FFC frame C, at approximately 112 ns.

Figure 6(b) shows two major pulses in the time-evolution of the x-ray emission recorded by the PCD detectors, which might suggest that there were also multiple bursts of the neutron and x-ray emission. However, the analysis of the clipped peaks in the nToF signal and their relative positions to the x-ray pulses in the PCD signal led us to conclude that the first clipped peak in the nToF signal was associated with the hard x-ray emission and the second with the neutron emission. The estimated time of both the hard x-ray and neutron emissions corresponded to the first x-ray peak in the PCD signal.

Other explanations could be ruled out assuming that the x-rays and neutrons were produced approximately at the same time. On the one hand, the first clipped peak in the signal from the far nToF detector could not be associated with the neutron emission because the time difference between its onset and the first PCD signal pulse was so short that it would imply relativistic neutron energies, which were unrealistic. On the other hand, the second clipped peak in the nToF signal could not originate from the hard x-rays because its onset, which we associated with the nToF signal dip, was so far away from the two PCD signal peaks that it would imply that the x-rays traveled from the source to the nToF detector slower than the speed of light. In addition, the delays of the nToF signal onsets between each other and from the first PCD pulse fit to the light travel times between the corresponding detectors. Therefore, we concluded that the onset of the x-ray emission in the nTOF signal corresponded to the first PCD pulse. However, due to the significant width of the x-ray clipped peak in the nTOF signal, the hard x-rays may have also been produced at the second PCD peak.

Due to the signal saturation, we could not derive the neutron energy spectrum. To estimate at least a lower bound on the highest energy neutrons detected, we first needed to determine whether the neutron emission in the nToF signal corresponded to the first or the second PCD peak. From the time differences between the dip of the nToF signal and the PCD peaks, we found that if the neutrons were emitted at the time of second PCD peak, then the neutron energy would be roughly equal to $\approx$30 MeV. This seems unrealistic because the energy of the incident deutron beams participating in the beam-target fusion would be in tens of MeV. Therefore, we concluded that the time of the neutron emission approximately coincided with the first PCD peak. As a result, we estimated that the highest energy neutrons detected were at least 4.1 MeV. Accordingly, the neutron energy corresponding to the delay of the center of the neutron peak was 2.3 MeV.

From the angular energy dependence of the neutrons produced in the beam-target $D(d,n)^3He$ fusion reaction on the energy of the incoming deuteron beams (see figure 7), assuming the target deuterium was stationary, it follows that the detected $\gtrsim$4.1 MeV fusion neutrons were generated by $\gtrsim$0.9 MeV deuteron beams. Such high deuteron energies were likely achieved via the ion acceleration mechanism discussed in this paper. Based on the transmissivity coefficient [35] for the x-rays passing through the 54 mm thick lead layer protecting the near nToF detector, the minimum energy of the hard

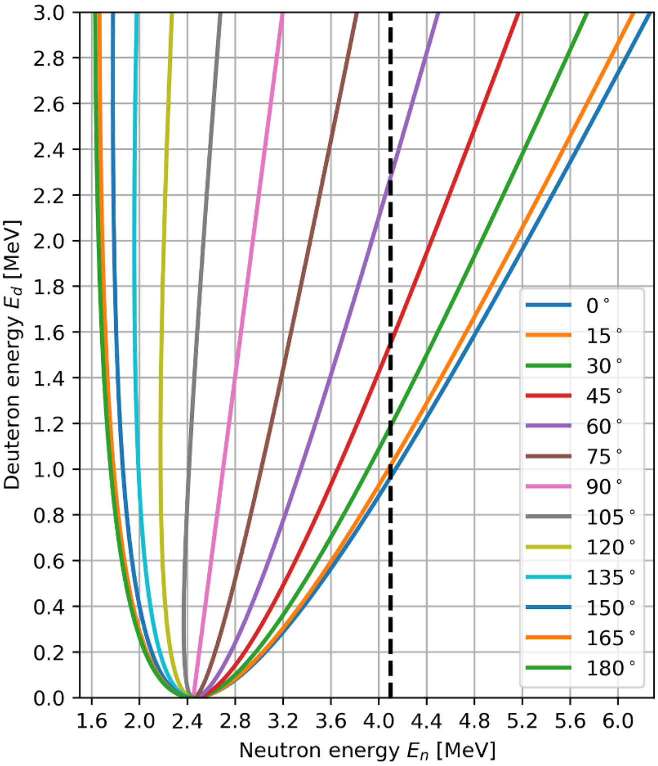

Figure 7. Angular dependence of the deuteron beam energy on the energy of the neutrons produced in the beam-target $D(d,n)^3He$ fusion reaction. The target deuterons are assumed to be stationary during the fusion reactions, and the angles are given by the directions of the incoming deuterons and outcoming neutrons in the laboratory frame. The dashed line corresponds to the neutron energy of 4.1 MeV measured by the far nToF detector.

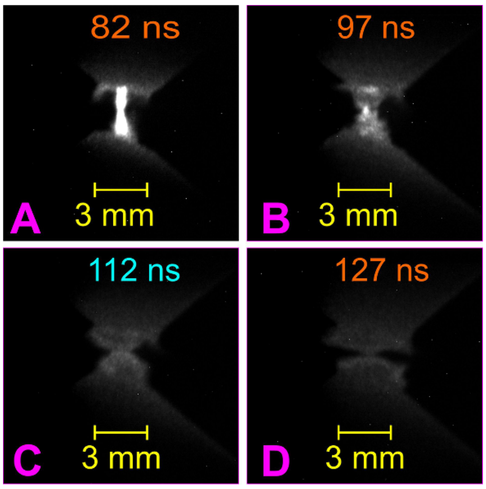

Figure 8. Visible light images of hybrid CD_2 fiber x-pinch captured by the fast frame camera (FFC).

x-rays was 0.6 MeV, which further supports the hypothesis of an acceleration mechanism because the hard x-rays originate in impacts of accelerated electrons with the electrode system.

Indirect evidence of the accelerated deuteron beams over the DD fusion protons was provided by FFC images (see figure 8), which captured the evolution of the hybrid X-pinch plasmas. Comparing their time stamps with the nTOF and

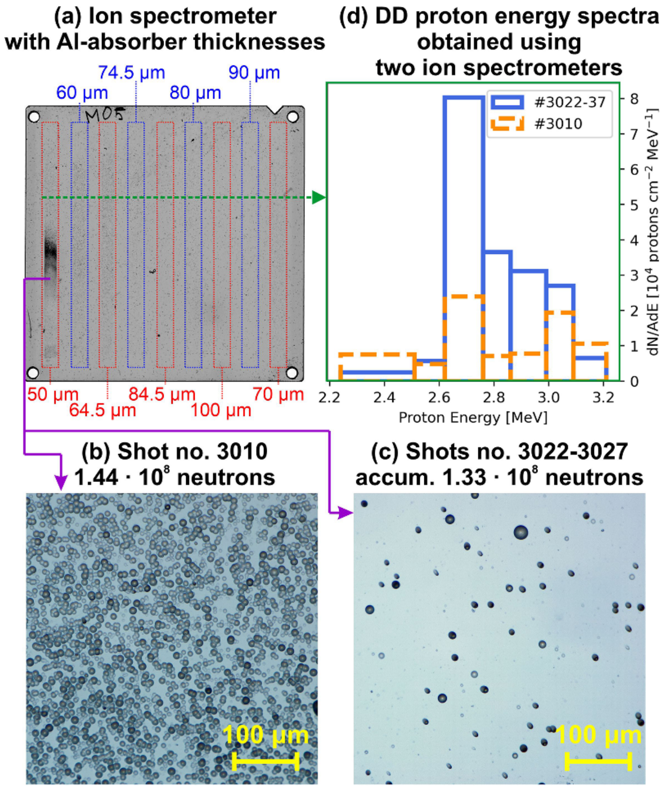

Figure 9. (a) CR-39 detector of the ion spectrometer in shot 3010. Individual bins on the CR-39 highlighted by dotted lines were shielded by Al strips of different thicknesses defining the energy ranges of detected ions. The first bin capturing an anisotropic and highly saturated ion signal corresponded to energy interval with a mean energy of ≈2.4 MeV in case of protons and ≈3 MeV in case of deuterons. (b) and (c) Comparison of microscopic photographs of tracks etched in two CR-39s used by the ion spectrometers for shot 3010 and during five shots from 3022 to 3027. The captured area lied near the saturated ion signal, as indicated by the purple arrows. The photo (c) shows much less tracks despite the fact that accumulated neutron yield during the five shots was comparable to the one in shot 3010. (d) Energy spectra of fusion DD protons measured in two ion spectrometers along the position of the green arrow highlighted in (a). The first was used for shot 3010 (in orange) and the second accumulated protons in shots from 3022 to 3027.

PCD signals in figure 6, we found that the estimated time of the x-ray and neutron emission at 111 ns nearly corresponds to the frame C at 112 ns. Interestingly, this FFC frame displays wide and weakly radiating necked plasma, contrasting with the narrow and highly radiating pinch shown in frame A at 82 ns. Therefore, it is likely that the detected ions were accelerated by the disruption of the deuterium plasma neck rather than from the beam-target fusion around the hot, dense carbon-deuterium plasmas of the hot-spot.

Additional evidence for the multi-MeV deuteron emission in shot 3010 was provided by the experimental results of the ion step-wedge-filter spectrometer (see figure 9). In this detector, a piece of CR-39 was protected by a plastic mask with several narrow windows (bins). In each window, the CR-39 was covered by an Al strip absorber of different thickness, which determined a lower energy threshold of the detected protons and deuterons. The thicknesses of Al filters were 50, 60, 64.5, 70, 74.5, 80, 84.5, 90, and 100 μm, which based on The-Stopping-Range-of-Ions-in-Matter (SRIM) tables [36] correspond to energy thresholds of 2.27, 2.54, 2.66, 2.78, 2.91, 3.04, 3.14, 3.26, and 3.48 MeV for protons or 2.87, 3.23, 3.38, 3.57, 3.71, 3.88, 4.02, 4.17, and 4.46 MeV for deuterons, respectively. Accordingly, the window-to-window variation of the ion fluence allows us to estimate the energy ranges of the protons and deuterons detected corresponding to each window of the ion spectrometer. In figure 9(a), we observe that the strong ion signal of the ion spectrometer was only under the 50 μm thick Al filter corresponding to >2.27 MeV protons or >2.87 MeV deuterons. The recorded ion signal was similarly anisotropic as in the deflectogram of the equally shielded CR-39 detector in the ion deflectometer, shown in figure 5(a). In the other windows covered by $\geqslant$60 μm Al filters, the strong ion signal disappeared and we detected only more uniform and low fluence ion background. It means that either the anisotropic ion beam hit only the first spectrometer's window but not any other, or that the energies of the detected protons or deuterons fit into the energy range of this specific spectrometer window, namely, 2.27–2.54 MeV for protons and 2.87–3.32 MeV for deuterons.

Both types of hydrogen ions probably contributed to the ion fluence in this ion spectrometer window, but our microscopic analysis of the CR-39 detector, shown in figure 9(a), proved that, in this shot, the number of accelerated deuterons predominated over the beam-target DD fusion protons. This analysis revealed that the number density of the individual etched ion tracks was much higher than the number of protons given by the estimated neutron yield. The number of fusion-produced protons should be the same as the number of the fusion neutrons due to the almost same probability of the two branches of the DD fusion reactions, i.e. $\mathrm{D(d,p)T}$ and $\mathrm{D(d,n)^3He}$. Therefore, a substantial number of ion tracks must have been created not by DD fusion protons but, most likely, by the accelerated deuterons. Figures 9(b) and (c) illustrate this by comparing images of an enlarged surface area of two CR-39 detectors. The former was used only in shot 3010, and the latter was used consecutively in five shots 3022 to 3027. Although the neutron yield in shot 3010 was comparable to the neutron yield accumulated during these five shots, the number of the etched ion tracks in shot 3010 was more than an order of magnitude higher.

All the evidence discussed above led us to conclude that the dominant ion signal captured in shot 3010 by the ion spectrometer (figure 9(a)) and the ion deflectometer (figure 5(a)) were predominantly produced by $\approx$3 MeV deuterons and that the DD-fusion protons contributed only to the secondary ion signal in the background. To estimate the energy of the proton background, we analyzed the etched tracks in the ion spectrometer used in shots 3022–3027. To investigate only the proton signal in shot 3010, we inspected the etched tracks that were far from the saturated region of the ion spectrometer, i.e. at the vertical position of the green horizontal line highlighted in figure 9(a). We found that for both spectrometers, the number of detected protons peaked at the energy of 2.7 MeV (see figure 9(d)), which we used as an estimate of the minimum detected proton energy for the rest of the ion diagnostics.

Since the ion deflections are inversely proportional to the ion momentum (see equation (3)) and thus to the square root of the beam energy, the uncertainty in the estimated proton and deuteron energies given by the energy range of the spectrometer window will not significantly influence the deflectometry measurements.

4.2. Measurements of the total pinch current

To measure the x-pinch current and further understand the behavior of the MeV deuteron beams in these experiments, we implemented the MAIZE's experimental setup illustrated in figure 3(a) into our numerical ion-tracking code written in Numpy Python and using the Just-In-Time compiler Numba for the algorithm parallelization.

In contrast with the ideally symmetric geometry assumed in section 2, the real experimental setup on MAIZE has several asymmetries, which were included in our numerical model to reflect the experimental setup realistically. Firstly, figure 3(b) shows that the conical electrodes were not perfectly concentric. This influenced the formation of the x-pinch plasma which was horizontally displaced by roughly 1.5 mm (see FFC images in figure 8). The significant horizontal displacement of the ion source can also be seen in the experimental data in figure 5 because they show that the D-grid shadows in both shots 3010 and 3012 as well as the pinhole holder's shadow in shot 3010 are closer to the left side of the CR-39 detector. Therefore, analyzing the experimental deflectograms, we estimated that the ion source was horizontally shifted from the center of the setup by $\approx 2 \pm 0.5$ mm. Accordingly, in addition to the size of the simulated ion source, we set its position as an input parameter for our numerical simulations.

Secondly, the B-fields were not azimuthally symmetric because the outer boundary of the B-field region was delimited by four return current rods influencing the B-field distribution in the x-y plane. Therefore, the mapped B-fields were not uniformly azimuthal and the ions detected by the ion deflectometer and the ion pinhole detector, shown in figure 4(a), situated close to the return current rods, were slightly affected by the local non-azimuthal B-fields. In our numerical model, simulated B-fields were generated by axial currents flowing through the surface of five ideal cylindrical conductors: a micro-z-pinch located within the edges of the tips of the conical electrodes and four return rods symmetrically arranged around the center of the geometry and with the opposite current polarity to the micro-z-pinch. The micro-z-pinch's location, size, and current were input parameters.

To determine ion displacements from the experimental data, we needed a reference 'no-deflection' ion image created without the influence of the B-fields by ballistic projection of the ion source onto the detector plane. To that end, we required an estimated position of the ion source. In particular, its vertical position was the most important due to the predominantly axial direction of the ion deflections. Assuming it is anywhere in the 2.8 mm anode-cathode gap between the cone tips would result in a significant error in the ion displacement measurements. To estimate the position of the ion source in the experiment, we used the shadows of the D-grid and pinhole

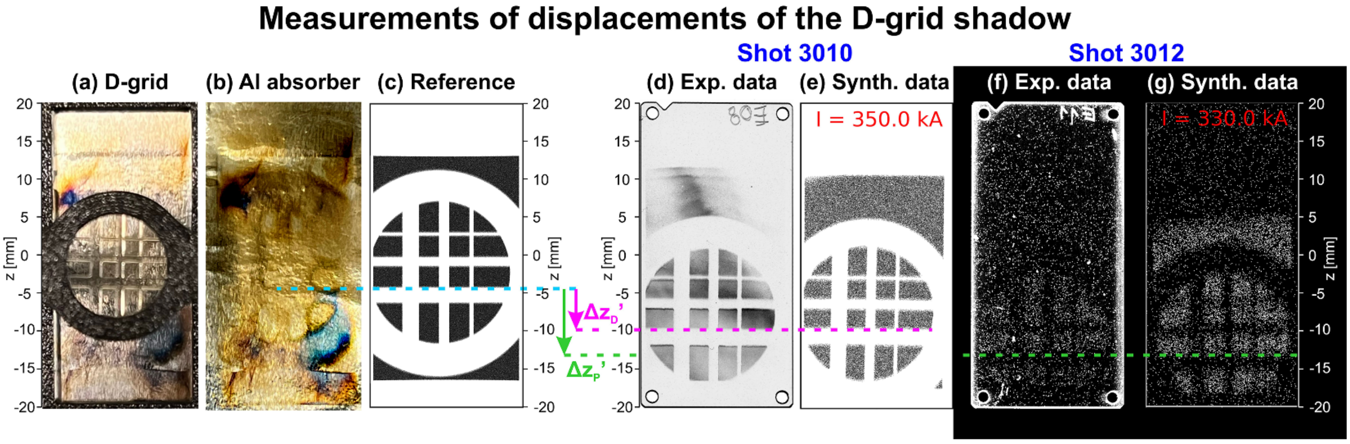

Figure 10. Measurements of D-grid shadow displacements in images of the ion deflectometers used in shots 3010 and 3012. (a) Front-view photo of the plastic D-grid holder of the ion deflectometer and the Al absorber covering the CR-39 detector. (b) Photo of the Al absorber in shot 3010 with the burned-in shadow of the D-grid on its surface. (c) The reference ion image which was reconstructed from the burned D-grid image on the Al absorber, and from which the D-grid shadow displacements can be determined. (d) Experimental 3 MeV deuteron deflectogram in shot 3010 showing the D-grid shadow displaced due to the ion deflections in the B-field. (e) Synthetic ion deflectogram obtained via numerical ion tracking simulations by fitting to the experimental deflectogram in shot 3010. (f) High-contrast and inversed experimental ion deflectogram in shot 3012 showing a faint D-grid shadow in the 2.7 MeV proton background. (g) Synthetic deflectogram in shot 3012 fit to the experimental data of the ion deflectometer. The axial displacement of the deuteron D-grid shadow is in magenta, the axial displacement of the proton D-grid shadow is in green.

holder that were burned into the surface of the Al absorbers used in shot 3010 in the ion deflectometer and in the ion pinhole camera, as shown in figures 10(b) and 12(b), respectively. The burn damage was most likely created by the heat of the plasma debris ejected after the total disruption of the x-pinch due to instabilities. Assuming that B-fields did not significantly affect the damaging plasma and that the source of the plasma debris was close to the ion source, we estimated that the ion source was in the middle of the anode-cathode gap within the ± 0.5 mm uncertainty, which correlates with the vertical position of the plasma neck observed in figure 8(c). The resulting reference image of the D-grid shadow is shown in figure 10(c). Note that the burned-in shadows on the Al absorbers are horizontally shifted similarly to the ion signals on the CR-39 detectors. This suggests that the location of the plasma source was indeed correlated with the location of the ion source.

Figure 10 demonstrates the axial displacements of the D-grid shadows of 3 MeV deuterons in shot 3010 and 2.7 MeV protons in shot 3012. We measured that the D-grid shadow shifts in these shots were equal to 5.4 ± 0.3 mm and 8.2 ± 0.4 mm, respectively. By fitting the estimated displacements of the D-grid shadows and the overall shape of the experimental data in figures 10(d) and (f), we used our numerical simulations to create synthetic deuteron and proton deflectograms for shots 3010 (figure 10(e)) and 3012 (figure 10(g)), respectively. The simulated ion beam in both shots were monoenergetic and had a uniform profile. The corresponding simulated ion trajectories are shown in figure 11. Based on our numerical simulations, we measured that the total load currents were 350 ± 30 kA for shot 3010 and 330 ± 50 kA for shot 3012.

The estimated current for shot 3010 was lower than the $\approx$390 kA circuit current measured by the Rogowski coil in the time of the first x-ray peak recorded by the PCD detectors (see figure 6). In contrast, the estimated value for shot 3012 was higher than $\approx$300 kA measured by the Rogowski coil during the x-ray peak (see [17]). The discrepancies in the estimated currents for deuterons and protons can be explained by the different durations and times of emission of these two hydrogen

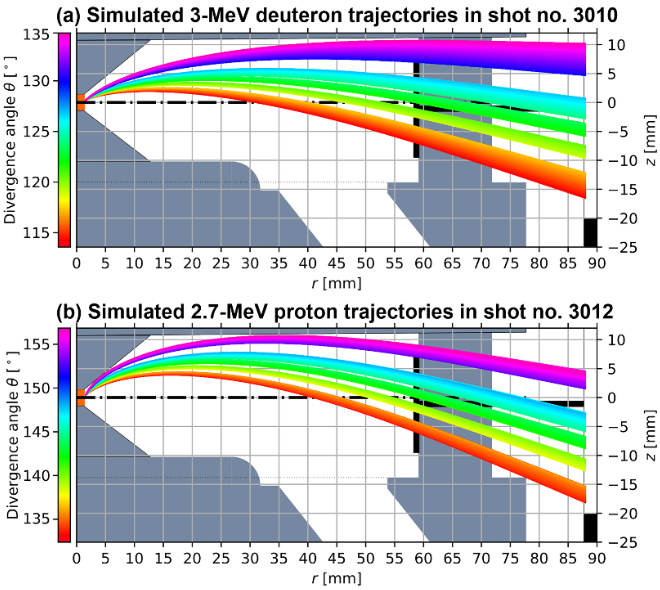

Figure 11. Simulated trajectories of the 3 MeV deuterons and the 2.7 MeV protons in hybrid x-pinch B-fields. The initial angles at which the simulated ion beams were emitted are indicated by the color of the individual trajectories. (a) Simulated trajectories of 3 MeV deuteron corresponding to the synthetic deuteron deflectogram in shot 3010. (b) Simulated trajectories of 2.7 MeV proton corresponding to the synthetic deuteron deflectogram in shot 3012. The initial (divergence) angles indicated are relative to the direction of the pinch current, which is in the negative direction of the z-axis.

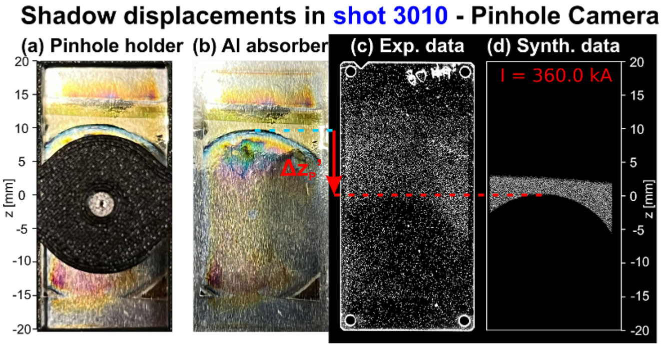

Figure 12. Measurements of displacements of the pinhole holder's shadow in the CR-39 image obtained by the pinhole camera detector in shot 3010. (a) Front-view photo of the plastic pinhole holder of the pinhole camera and the Al absorber covering the CR-39 detector. (b) Photo of the Al absorber with the burned-in shadow of the pinhole holder on its surface. (c) Experimental and (d) synthetic 2.7 MeV proton deflectograms showing the pinhole holder shadow displaced due to the proton deflections in the B-field.

ion species. The E-fields that accelerated the deuteron beams to energies of 3 MeV must have been very short in duration relative to the E-fields that accelerated the deuteron beams responsible for the beam-target DD fusion protons.

The estimated uncertainties of the measured currents predominantly originated from the uncertainty in the locations of the ion source and the pinch axis, and from the uncertainty of the placement of the CR-39 detectors inside the ion diagnostics. However, our simulations revealed several additional bounding conditions of the simulated system that allowed us to find the most reliable fit. For shot 3010, the relative vertical position of the ion source to the ion detector was in our simulations found not only from the burned-in D-grid images on the Al absorbers but also from the vertical position of the anode plate, whose shadow determined the upper edge of the synthetic deflectogram shown in figure 10(e). Furthermore, based on the estimated thickness of the thinnest gridline in the experimental deflectogram, we inferred that the 3 MeV deuteron source in shot 3010 was $\approx$0.6 mm tall and $\approx$0.2 mm wide, while the 2.7 MeV source in shot 3012 was $\approx$0.8 mm tall and $\approx$0.5 mm wide. If the error of the current measurements were caused only by the size of the ion source, it would be $\pm$10 kA in the case of the deuteron image in shot 3010 and $\pm$20 kA in the case of the proton image in shot 3012.

In our simulations, it was necessary to place the ion source at the outer radial edge of the conical electrode tips; otherwise, the emitted ions hit the anode or were too deflected to reach the ion detector. This results from the required initial divergence of the emitted ions, which they needed to compensate for their subsequent deflections to reach the ion detector (see the simulated ion trajectories in figure 11). The relative horizontal position of the ion source in the parallel direction to the detector plane was chosen not only by the shift of the ion signal to the left side of the CR-39 detector but also by its relative position to the return current rods. Since the distance from the outer edge of the closest return current rod to the D-grid holder was 10 mm and to the ion beam axis 18 mm, local B-fields around this current rod slightly rotated ions and the ion deflectogram in the detector plane (see figure 10(g)). Furthermore, we found that the specific B-field profile and the pinch radius had only limited effect on the current measurements due to the small pinch cross-section, assuming there were no significant currents radially outside the outer edge of the conical electrode tip. In contrast, the location of the pinch axis, which we assumed to be different from the axis of the ion source, had a more significant effect on the ion trajectories because it determined the magnitude of the B-fields along the entire ion trajectory. When the axis of the pinch with a small radius was placed in our simulations too close to the ion source, deflections of emitted ions were too strong to reach the ion detector. Therefore, we estimated that the location of the ion source was $\approx$1 mm from the pinch axis.

In addition to the results of the ion deflectometers, figure 12 displays the axial displacement of the pinhole holder's shadow in 2.7 MeV proton signal in shot 3010, which we measured to be 9.2 ± 0.5 mm. Using numerical simulations, we estimated that the total current during the proton emission in shot 3010 was equal to 360 ± 50 kA, which corresponds to the current estimated from the synthetic deuteron deflectogram in the same shot (see figure 10(e)). Note that the upper part of the synthetic proton deflectogram in figure 12(d) does not correspond to the experimental data shown in figure 12(c). The recorded ion tracks in the upper part of the CR-39 detector may be from less deflected ions, which might be caused by the significantly larger proton source or the time-varying current during the proton emission.

4.3. The angular distributions of simulated deuteron and proton beams

Figures 11(a) and (b) show simulated trajectories of 3 MeV deuterons and 2.7 MeV protons corresponding to the synthetic deflectograms in shot 3010 and 3012 shown in figures 10(e) and (g), respectively. To compensate for their magnetic deflections, the beams of both ion species were emitted at large divergence angles θ with respect to the pinch current direction, which is in the negative direction of the z-axis. Ions emitted at even larger angles would hit the anode plate and could not be detected. Ions emitted at smaller angles than those displayed would drop too quickly and also would not be able to reach the ion detector. Nevertheless, the divergence angles θ retrieved from the ion simulations, which are greater than 90°, imply that both ion species were emitted in a direction that is largely opposite to that of the pinch current.

In the case of the 2.7 MeV protons, the observed directions can be explained by the angular dependence of the energy of the protons produced in the beam-target DD fusions, as shown in figure 13. This figure demonstrates that the fusion protons are emitted with a certain probability in every direction, but their energy depends on the emission angle and the energy of the deuteron 'beam' hitting the deuterium 'target'.

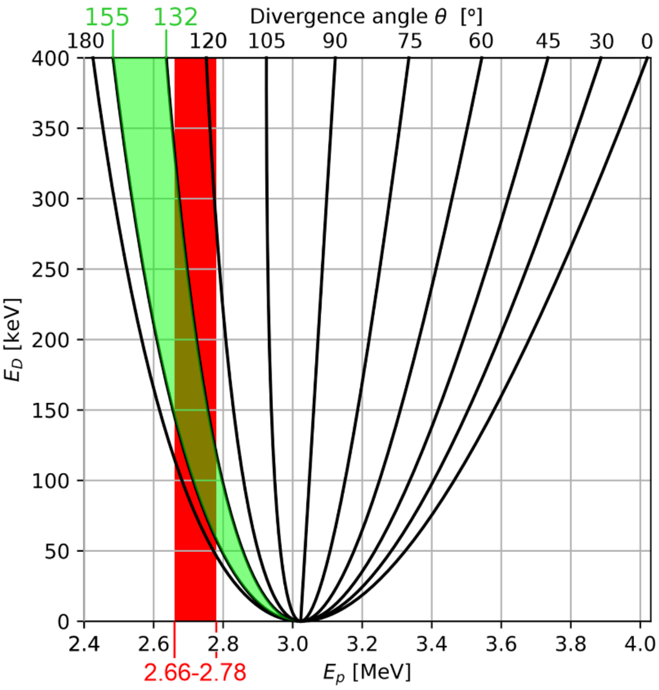

Figure 13. Angular energy distribution of 'beam' deuterons $E_D(E_p, \theta)$ hitting stationary 'target' deuterons. The distribution is a function of the proton energy E_p and the proton emission angle θ of beam-target fusion protons. The red area corresponds to the third bin in the spectrometer, with the peak of fusion protons centered at ≈2.7 MeV. The lime area corresponds to the calculated emission angles of simulated proton trajectories.

Therefore, the fusion protons emitted at angles greater than 90° have energies less than the 3 MeV of energy released from the DD fusion reaction. Moreover, it follows from the range of the proton divergence angles estimated from the numerical simulations (the lime area in figure 13) and the proton energies estimated from the ion spectrometer (the red area) that the 'projectile' deuteron energy was 150 ± 50 keV. This suggests that the estimated divergence roughly agrees with the measured proton energy because the 'projectile' deuterons with energies close to this energy estimate have the highest cross-section $\sigma(E_D)/E_D$ of the fusion reaction D(d, p)T related to the deuteron energy [37].

In the case of the 3 MeV deuterons, the explanation of the large initial divergence angles is difficult and probably beyond the scope of this paper, because our numerical simulation code implements only a simplified model of a source of monoenergetic (already accelerated) deuterons. In reality, the deuteron beams are accelerated by E-fields and, at the same time, deflected by B-fields in the region of the ion source. One possible explanation is the presence of a radial electric field that could balance the magnetic deflections and deflect ions radially towards the ion detector. Our experiments with hybrid gas-puff z-pinch GIT-12, presented in [12], hinted at the existence of a radial E-field. This was based on the experimental results of the ion beam-profile detector, which indicated incident angles of detected 20 MeV deuterons reaching up to 70°. However, significantly more experimental data are required to support this hypothesis.

5. Conclusions and future prospects

This paper presents further development of ion deflectometry in z-pinches by implementing it on a mid-size university device for the first time and providing the proof of concept for generating multi-MeV ions for self-sustained point-projection deflectometry measurements in z-pinches. The hybrid x-pinch carbon-deuterium plasma driven by the MAIZE LTD generator at ≈500 kA was capable of producing the 2.7 MeV proton emission via DD fusion reactions in multiple shots. In shot 3010, with the neutron yield of 1.4×10^8, two species of hydrogen ions with MeV energies were produced from a sub-mm source. Besides 2.7 MeV DD protons (which, due to beam-target dynamics, were down-shifted in energy from the standard 3.02 MeV that occurs in the DD reaction's center-of-mass rest frame), highly anisotropic 3 MeV accelerated deuteron beams were observed with temporally short emission durations. The radial direction of these beams suggests an unidentified mechanism for deflecting ions to large divergence angles. Based on the numerical simulations reproducing the experimental proton and deuteron images, the total pinch current was estimated in shots 3010 and 3012 to be 350 ± 30 kA and 330 ± 50 kA, in reasonable agreement with the total current measured by MAIZE's Rogowski coil.

The reproducible emission of MeV protons from a localized source opens the possibility of using the z-pinch-driven ion backlighting to probe other high-energy-density plasma objects. For example, the localized source of MeV hydrogen ions in the center of a fast MA pulsed-power generator might be used for ion imaging of a secondary z-pinch situated in the return current circuit. In closing, we note that detecting MeV deuteron beams accelerated into large divergence angles will, in general, help us better understand the ion acceleration mechanisms occurring in z-pinches and ion diodes.

Data availability statement

All data that support the findings of this study are included within the article (and any supplementary files).

Acknowledgments

This research has been supported by the Grant Agency of the Czech Republic (Grant No. 23–04679S), and the Czech Technical University in Prague (Grant No. SGS22/161/OHK3/3T/13). The UM team was supported by the U.S. DOE Office of Science Early Career Research Program under Grant DE-SC0020239, and by the Center for Magnetic Acceleration, Compression, and Heating (MACH), part of the U.S. DOE-NNSA Stewardship Science Academic Alliances Program under Cooperative Agreement DE-NA0004148.

ORCID iDs

Vojtech Munzar https://orcid.org/0000-0001-8863-6270
George Dowhan https://orcid.org/0000-0001-7963-4361

Daniel Klir https://orcid.org/0000-0002-0510-3653
Jan Novotny https://orcid.org/0000-0002-4703-6022
Karel Rezac https://orcid.org/0000-0002-2002-2886
Jakub Cikhardt https://orcid.org/0000-0002-8222-8038
Balzima Cikhardtova https://orcid.org/0000-0003-3636-2794
Nicholas Jordan https://orcid.org/0000-0001-9518-4284
Pavel Kubes https://orcid.org/0000-0003-1356-8765
Jakub Malir https://orcid.org/0000-0002-4129-7977
Landon Tafoya https://orcid.org/0000-0002-0108-6200
Karel Turek https://orcid.org/0000-0002-3698-2785
Ryan McBride https://orcid.org/0000-0002-5022-9749

References

[1] Schaeffer D B *et al* 2023 *Rev. Mod. Phys.* **95** 045007
[2] Macchi A, Borghesi M and Passoni M 2013 *Rev. Mod. Phys.* **85** 751
[3] Cecchetti C *et al* 2009 *Phys. Plasmas* **16** 043102
[4] Li C *et al* 2008 *Phys. Rev. Lett.* **100** 225001
[5] Sutcliffe G, Pearcy J, Johnson T, Adrian P, Kabadi N, Pollock B, Moody J, Petrasso R and Li C 2022 *Phys. Rev.* E **105** L063202
[6] Manuel M J-E, Sinenian N, Séguin F, Li C, Frenje J, Rinderknecht H, Casey D, Zylstra A, Petrasso R and Beg F 2012 *Appl. Phys. Lett.* **100** 203505
[7] Mariscal D *et al* 2014 *Appl. Phys. Lett.* **105** 224103
[8] Beg F N 2013 *Technical Report* UCSD 2009-0512 University of California San Diego (https://doi.org/10.2172/1093880)
[9] Munzar V *et al* 2021 *Phys. Plasmas* **28** 062702
[10] Klir D *et al* 2018 *New J. Phys.* **20** 053064
[11] Klir D *et al* 2020 *Plasma Phys. Control. Fusion* **62** 035009
[12] Klir D *et al* 2020 *New J. Phys.* **22** 103036
[13] Suzuki-Vidal F *et al* 2013 *New J. Phys.* **15** 125008
[14] Klir D *et al* 2020 *Matter Radiat. Extremes* **5** 026401
[15] Gilgenbach R *et al* 2009 *AIP Conf. Proc.* **1088** 259–62
[16] McBride R *et al* 2018 *IEEE Trans. Plasma Sci.* **46** 3928
[17] Dowhan G *et al* 2024 Neutron Generation in a Deuterated-Polyethylene-Fiber Hybrid X-pinch on the MAIZE LTD *IEEE Trans. Plasma Sci.* (8th Special Issue on Z-Pinch Plasmas) submitted
[18] Nürnberg F *et al* 2009 *Rev. Sci. Instrum.* **80** 033301
[19] Devic S 2011 *Phys. Medica* **27** 122
[20] Das I J 2017 *Radiochromic Film: Role and Applications in Radiation Dosimetry* (CRC Press) (https://doi.org/10.1201/9781315154879)
[21] Cartwright B G, Shirk E and Price P 1978 *Nucl. Instrum. Methods* **153** 457
[22] Cassou R and Benton E 1978 *Nucl. Track Detect.* **2** 173
[23] Munzar V, Klir D, Cikhardt J, Cikhardtova B, Kravarik J, Kubes P and Rezac K 2018 *IEEE Trans. Plasma Sci.* **46** 3891
[24] Pikuz S A, Shelkovenko T A and Hammer D A 2015 *Plasma Phys. Rep.* **41** 291
[25] Shelkovenko T, Pikuz S, Tilikin I, Mitchell M, Bland S and Hammer D 2018 *Matter Radiat. Extremes* **3** 267
[26] Lebedev S, Beg F, Bland S, Chittenden J, Dangor A, Haines M, Zakaullah M, Pikuz S, Shelkovenko T and Hammer D 2001 *Rev. Sci. Instrum.* **72** 671
[27] Shelkovenko T, Pikuz S, Mingaleev A and Hammer D 1999 *Rev. Sci. Instrum.* **70** 667
[28] Grabovskii E, Mitrofanov K, Oleinik G and Porofeev I Y 2004 *Plasma Phys. Rep.* **30** 121
[29] Zhao T, Zou X, Wang X, Zhao Y, Du Y, Zhang R and Liu R 2010 *IEEE Trans. Plasma Sci.* **38** 646
[30] Shelkovenko T, Pikuz S, Cahill A, Knapp P, Hammer D, Sinars D, Tilikin I and Mishin S 2010 *Phys. Plasmas* **17** 112707
[31] Shelkovenko T A *et al* 2015 *Plasma Phys. Rep.* **41** 52
[32] Collins G, Valdivia M, Hansen S, Conti F, Carlson L, Hammer D, Elshafiey A, Narkis J and Beg F 2021 *J. Appl. Phys.* **129** 073301
[33] Apfel R E and Roy S 1984 *Nucl. Instrum. Methods Phys. Res.* **219** 582
[34] Zhang G *et al* 2011 *Appl. Radiat. Isot.* **69** 1453
[35] Hubbell J H and Seltzer S M 1995 *Technical Report* PB-95-220539/XAB; NISTIR-5632 National Inst. of Standards and Technology (https://doi.org/10.18434/T4D01F)
[36] Ziegler J F, Ziegler M D and Biersack J P 2010 *Nucl. Instrum. Methods Phys. Res.* B **268** 1818
[37] Chadwick M *et al* 2006 *Nucl. Data Sheets* **107** 2931